Enhancing Ground-Based SAR Monitoring With PCA-Based Geometry Transformation for Improved Phase Unwrapping

Matthieu Rebmeister, Andreas Schenk, Stefan Hinz, Frédéric Andrian, and Maxime Vonié

***Abstract*—Ground-based synthetic aperture radar (GB-SAR) systems are most often used for landslide and open-pit mine monitoring due to their high temporal sampling and spatial coverage. For infrastructure monitoring, it has not yet attained widespread adoption for this purpose, mainly due to the complex imaging geometry and related challenges for phase unwrapping. In case of vertical structures, the GB-SAR projection geometry induces strong layover and foreshortening that may be difficult to handle during phase unwrapping. In this letter, we present an approach based on principal component analysis to transform the GB-SAR interferograms into a suitable geometry, to ease the phase unwrapping, making it more efficient and more robust against unwrapping errors. The method is tested on a distorted imaging scenario at the Enguri Dam in Georgia. The results show a strong improvement of the phase unwrapping and encourage the usage of this method in the case of interferometric analysis of strongly distorted SAR images. Depending on the scenario, the subsequent required filtering may remove local deformation patterns, but considerably increases the consistency of the global displacement pattern. Two displacement maps after correction for atmospheric and repositioning influences are presented and compared with a numerical simulation based on a model calibrated with the plumblines inside the dam. The comparison shows an overall good agreement between numerical simulations and the displacement maps.**

***Index Terms*—Dam monitoring, ground-based synthetic aperture radar (GB-SAR), InSAR, phase unwrapping, principal component analysis (PCA).**

I. Introduction

TRADITIONAL methods of infrastructure monitoring, such as geodetic networks, laser scanners, and pendulums/collimators [1] have limitations in terms of time consumption, cost, and the level of detailed information they can provide. To overcome these challenges, ground-based synthetic aperture radar (GB-SAR) has emerged as a powerful alternative for infrastructure monitoring and was first applied in [2]. GB-SAR offers unique capabilities for remote and nondestructive assessment, thanks to its high sampling rate and dense spatial coverage. Moreover, even if the accuracy in the millimeter order [3] is lower than the classical plumblines, it is sufficient for structure monitoring in many cases. While it has become a common tool for landslide and open-pit mine monitoring, its application for dam observation has not yet achieved widespread adoption. In [4], [5], and [6], several challenges that hinder the fully automatic and reliable usage of GB-SAR for dam observation were identified. Some pipelines were presented in [7] and [8] to observe very small deformations of the dam with a GB-SAR but on overall time stamps shorter than four days.

One of the challenges is the highly inadequate dam geometry for GB-SAR measurements. Due to the verticality of dams and the projection equations of the GB-SAR, the images are affected by strong layover and foreshortening that can lead to difficulties for the signal processing. Even using planning tools like in [9], it would be impossible to find a station location that is not strongly affected by the SAR distortions. However, this first challenge is solved in [10] by introducing a Bayesian geocoding.

Still, a major remaining challenge in GB-SAR monitoring is the reliable unwrapping of phase information obtained from the interferometric data. Phase unwrapping is a critical step in the data processing pipeline as it aims to extract absolute displacement values from wrapped phase differences [11]. In continuous monitoring, the challenge is smaller due to the high temporal sampling. For epochwise monitoring, i.e., solely 2-D scenarios, different methods exist, with the statistical-cost, network-flow algorithm for phase unwrapping (SNAPHU) [12] being the most used algorithm in the context of SAR interferometry. In case of acquisitions with several months in between, the complex geometry of infrastructures poses a substantial problem. The presence of backscatter points from strongly varying elevation in neighboring cells or even in the same resolution cell can lead to difficulties during the phase unwrapping process. As the existing unwrapping algorithms are designed mainly for spaceborne SAR images, they rely on a predominantly 2-D geometry of the imaged terrain. However, in cases of steep slopes or even vertical structures, the classical *azimuth-range* geometry is likely to result in extreme distortions. Moreover, the imaging of concave arch dams is a special challenge, as it can introduce an inversion of fringe patterns. Therefore, classical workflows

Received 5 November 2024; revised 20 January 2025; accepted 8 February 2025. Date of publication 26 February 2025; date of current version 21 March 2025. This work was supported in part by the BMBF (Bundesministerium für Bildung und Forschung) and in part by the DAMAST-Transfer project (Dams and Induced Seismicity). *(Corresponding author: Andreas Schenk.)*

Matthieu Rebmeister was with the Institute of Photogrammetry and Remote Sensing, Karlsruhe Institute of Technology, 76128 Karlsruhe, Germany. He is now with the Leica Geosystems - Part of Hexagon, 9435 Heerbrugg, Switzerland (e-mail: matthieu.rebmeister@leica-geosystems.com).

Andreas Schenk and Stefan Hinz are with the Institute of Photogrammetry and Remote Sensing, Karlsruhe Institute of Technology, 76128 Karlsruhe, Germany (e-mail: andreas.schenk@kit.edu).

Frédéric Andrian and Maxime Vonié are with the Artelia, Grenoble, 38130 Echirolles, France (e-mail: frederic.andrian@arteliagroup.com).

Digital Object Identifier 10.1109/JSTARS.2025.3542115

considering the geocoding only after the interferometric processing, as for example the one given in [13], present limitations. To optimize the application of a 2-D unwrapping algorithm, a suitable mapping to a minimal undistorted imaging geometry needs to be found. Indeed, working in a transformed geometry can improve the quality and reliability of phase unwrapping, as described in [14] for spaceborne SAR. In the latter work, the phase filtering and unwrapping are realized in the map geometry (i.e., *longitude-latitude*) and not in the slant-range geometry, which showed valuable improvements in complex mountainous areas. Indeed, in mountainous areas, the slope of the terrain can have a similar orientation as the wavefront of the SAR signal, leading to extreme foreshortening in the *azimuth-range* system. As the goal is to work in a coordinate system that minimizes the foreshortening without suffering from layover, the *longitude-latitude* system is clearly not adequate for monitoring a vertical structure. For GB-SAR we are looking for an optimum mapping with minimum foreshortening and layover effects.

The rest of this letter is organized as follows. Section II describes the problem encountered when observing complex infrastructures with a GB-SAR and the case study. Section III presents the methodologies used for the geometric transformation. Section IV analysis the improvement made using the proposed method compared to the classical unwrapping geometry. Finally, Sections V discusses the transferability of the method and proposes some further investigations. Finally, Section VI concludes this letter.

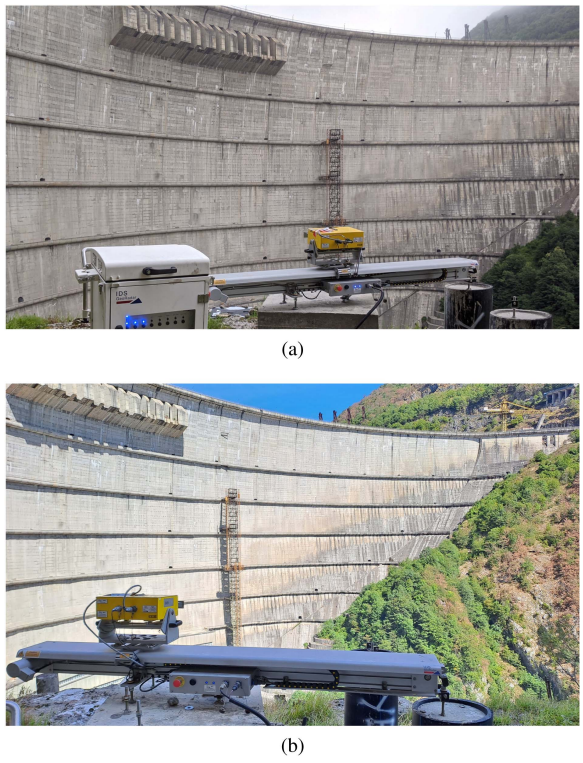

(a)

(b)

Fig. 1. Case study at Enguri Dam in Georgia. (a) First point of view oriented toward the central part of the dam. (b) Second point of view oriented toward the surrounding rocks.

II. Problem Description

A. Dataset Presentation

The case study is the Enguri Dam in Georgia, which stands at a towering height of 271.5 m and a developed length of 800 m at the crest. This dam ranks as the fifth largest arched dam currently in operation. From a geometric perspective, it is characterized as a double-arched dam, exhibiting a parabolic shape both in the horizontal plane and in elevation. Five separate measurement campaigns were conducted between June 2021 and March 2023. The sensor employed for these measurements is a GB-SAR, which acquires signals in the Ku-band with a wavelength of $\lambda = 17$ mm, and a range and cross-range resolution of 0.75 m and 0.25°, respectively. The station's installation site is located near the dam, ensuring the delivery of highly accurate and spatially dense point observations. Fig. 1 provides a visual representation of the station locations. The main station is the one in Fig. 1(a), because it has almost the full dam in visibility. The second point of view presented in Fig. 1(b) has the same phase center, but looks at the right part of the dam, as well as the surrounding rocks. This station will be used only in the last part of the letter to correct the atmospheric and repositioning errors.

To eliminate coregistration issues and minimize repositioning errors between the measurement campaigns, a concrete foundation was constructed. For each epoch-measurement, hundreds of single look complex (SLC) images have been captured. In addition, a georeferenced 3-D point cloud model of the dam is at our disposal. The accuracy of the ground control points and check points is 10 and 15 cm, respectively. The position and orientation of the sensor with respect to this model are calibrated using corner reflectors installed on the structure, which are subsequently identified in the SAR images. This process enables subpixel orientation accuracy, crucial for the geocoding, as pointed out by [15].

B. Data Preprocessing

First, the selection of persistent scatterers (PS) [16] is accomplished using two criteria. The first one is the amplitude dispersion (D_A) as defined in [17], which serves as an initial estimate of the phase noise. The second criterion employs the coherence γ and is computed using the nonlocal multitemporal interferometry based on amplitude similarity method presented in [18], which provides a robust coherence estimator for the SAR image stack. PS are selected based on the following thresholds: $\gamma > 0.6$ and $D_A < 0.35$. The result of this step is a set of N_{PS} complex values for each campaign. Their coordinates in the SAR geometry are given by: $\mathbf{x}_{\text{PS}} = [x_{\text{PS},k}, y_{\text{PS},k}]_{k\in[1:N_{\text{PS}}]} \in \mathbb{R}^2$. The output localization of the points is shown in Fig. 3 for the installation shown in Fig. 1(a). Each line of the latter figure corresponds to an interferogram with a different baseline. The first case presents a moderate number of fringes, the second a high number, and the last corresponds to the simplest case, with only one visible phase jump.

Subsequently, an averaged acquisition is computed for each epoch to enhance the signal-to-noise ratio. As several hundred of SLC images are available, an analysis based on averaged amplitude dispersion is conducted to select the optimal set of

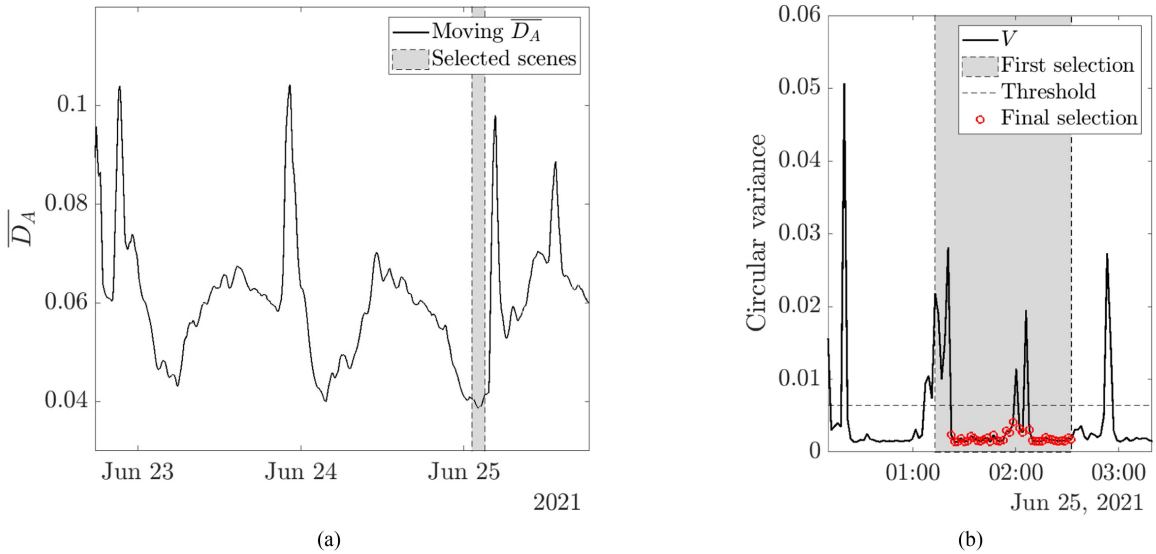

Fig. 2. Scene selection for the first campaign based on (a) moving amplitude dispersion and (b) circular variance on the selected PS points for a refined and more sensitive selection.

SLC images. Considering a single epoch, the quality of each scene n is evaluated with the mean amplitude dispersion $\overline{D_A}(n)$ over a surrounding temporal window of odd size W, computed as follows:

$$\overline{D_A}(n) = \frac{1}{N_{\text{PSC}}} \sum_{k=1}^{N_{\text{PSC}}} \frac{\sigma_A(k,n)}{\mu_A(k,n)} \tag{1}$$

with $\mu_A(k,n)$ the mean amplitude for point k over the window centered on the acquisition n and of size W, and $\sigma_A(k,n)$ the corresponding standard deviation. In this work, the chosen size of W is one hour. For the first epoch, the moving average of mean amplitude dispersion is illustrated in Fig. 2(a). Afterwards, the index of the central scene to be averaged for the campaign p is given by

$$I_p = \text{argmin}_n \left(\overline{D_A}(n)\right). \tag{2}$$

This first criterion is based on a smoothed temporal quantity. The circular variance of each scene $V(n)$ defined in [19] is used as a second step to refine the selection process. This metric is calculated on sequential interferograms to depict the dispersion of the phase values around the mean of each interferogram. Then, the standard deviation σ_V of V is computed with all the scenes in the segment $[I_p - (W-1)/2\,; I_p + (W-1)/2]$ and is used as a threshold to delete all the scenes, where $V > \sigma_V$. After that, the scenes used for the average computation are given by the set $\mathcal{S}_e$

$$\mathcal{S}_e = \left\{ n \in \left[I_p - \frac{W-1}{2};\, I_p + \frac{W-1}{2} \right] \mid V(n) < \sigma_V \right\}. \tag{3}$$

The set $\mathcal{S}_e$ is marked by the red dots in Fig. 2(b). Finally, the mean acquisition $\mathbf{z_p} = \{z_p(k)\}_{k\in[|1\,;N_{\text{PSC}}|]}$ is computed for each campaign via

$$z_p(k) = A_p(k)e^{i\varphi_p(k)} = \frac{1}{|\mathcal{S}_e|} \sum_{n\in\mathcal{S}_e} z(k,n) \tag{4}$$

with $z(k,n)$ the SLC value of acquisition n at point k.

The following step involves the geocoding to determine the 3-D coordinates of the observed coherent points on the SAR images. This step is particularly challenging when dealing with infrastructures and the specific geometry of GB-SAR acquisitions, due to the layover and foreshortening. As presented in [20], the resolution cells in a GB-SAR pixel are built by the intersection of cones in azimuth and spheres in range. Therefore, signals originating from structures with a similar planar localization but varying heights are summed up within the same resolution cell. This point does not play a significant role in the main GB-SAR applications, such as landslides and open-pit mines monitoring [21]. As we will transform the geometry based on the 3-D location of the PS, the geocoding must be done with high precision. The maximum a posteriori (MAP) combined with the ray tracing method developed in [10] is applied on the available external 3-D model. The density of the resulting point cloud is considerably higher than that of the GB-SAR, with a point separation set to 15 cm. For each pixel, it enables the identification of the 3-D points that have the highest probability of contributing to the observed signal based on an intensity model. To enhance the spatial density of the points, the geocoding is not applied using a single set of 3-D coordinates for each pixel, but to all points of the 3-D model having a probability higher than a given threshold. This probability is based on an intensity model using the antenna pattern and the incidence angle, and can be seen as a forward model of the tomographic approach. The phase value assigned to each of these points is that of the considered pixel. This step results in a new number of points, $N_{\text{geo.}} > N_{\text{PS}}$, still with N_{PS} unique phase values. This technique

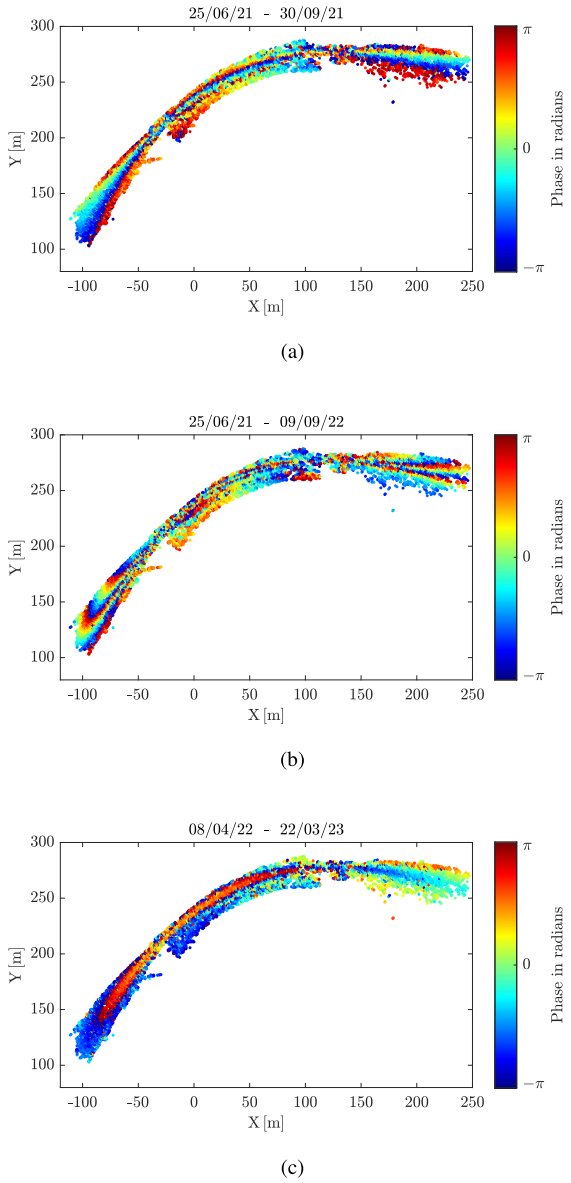

Fig. 3. Three interfoergrams after the PSC selection. (a) Between June 2021 and September 2021. (b) Between June 2021 and September 2022. (c) Between April 2022 and March 2023.

is applied for two main reasons. First, the acquisition geometry of the GB-SAR onto the dam leads to strong foreshortening. Therefore, a pixel can represent several meters and up to 150 m of the dam in elevation in the presented case. It is not realistic to project the phase value on a single point, but rather on the most probable surface that sends the signal back. Second, the 3-D map will present fewer holes, helping with the phase unwrapping, but still with a strong aliasing. The latter effect is smoothed with the subsequent spatial filtering step.

C. Geometric Analysis

The raw interferogram between the two considered epochs shown in Fig. 3(a) reveals the effect of foreshortening and layover, which can be studied in Fig. 4(a). The simulated plot on the left side of the figure is the result of the developed ray tracing algorithm P-RaySAR [10] which helps to understand the strong layover and inversion of the elevation gradient in the SAR geometry. Specifically, the left, right, and central segments of the dam display a noticeable phase gradient, that can be linked to the elevation of the points. On the left and right parts of the dam, the height increases with increasing distance from the sensor. However, within the central segment of the dam, even with tightened fringes, the height shows the reversed trend, with decreasing values for increasing distance from the GB-SAR. Consequently, two distinct nodes can be identified in the acquisitions, where the radar backscatter from the entire vertical column of the dam is foreshortened into one image pixel. Therefore, a reversal occurs in the relative range positioning of the PS with respect to their elevation. A zoom in to one of these nodes with the given GB-SAR resolution cells is also provided.

To better understand the phase gradient inversion, a study of the elevation gradient with respect to the range coordinate $\nabla_r Z = dZ/dr$ is conducted. A grid of points on the dam is created, with a spacing of 10 m, and corresponding to the field of view of the system. Subsequently, those points are regrouped by similar cross-range angle θ and the gradient $\nabla_r Z$ is computed between neighboring points for each bin. The median of those gradients is computed for each bin and represented in Fig. 4(b). To improve the visibility, a moving average with respect to the cross-range angle θ is also displayed. The depicted phenomenon on the interferogram is confirmed by the two changing points of the gradient sign. As the atmospheric and deformation signals are highly correlated with the height, a fringe inversion is observed on the interferogram. Fig. 4(b) expresses that the phase gradients have the same direction on the left and right sides of the dam, but it is inverted in its center. This phenomenon is clearly visible in Fig. 3(a).

Fig. 4 also enables to clarify the layover and foreshortening effects present in the scenario. The sides are expressing foreshortening but without layover. Therefore, the observed signal fringes express the displacement and atmospheric change with a strong spatial compression. Each pixel contains the average value of the foreshortened area, which means that the ground resolution is much lower than the slant resolution. For the central part, foreshortening and layover are occurring. However, the raw interferogram fringes in Fig. 3(a) are interpretable. In fact, the layover concerns only the central part of the dam between $x = 0$ m and $x = 120$ m. Considering a range distance to the radar of less than 300 m in this area, a vertical antenna aperture angle of 30° and an inclined viewing angle of $+5^\circ$ for the GB-SAR, only contributions from points with a height greater than 50 m with respect to the GB-SAR position can be imaged in the central part of the dam even with conservative assumptions. Thus, only the upper part of the layover is significantly contributing to the observed signal.

III. Unwrapping in the Optimal Geometry

The transformation process is based on the methodology described in [22]. Its adaptation and application to GB-SAR processing is described in detail in [23]. It involves the structure

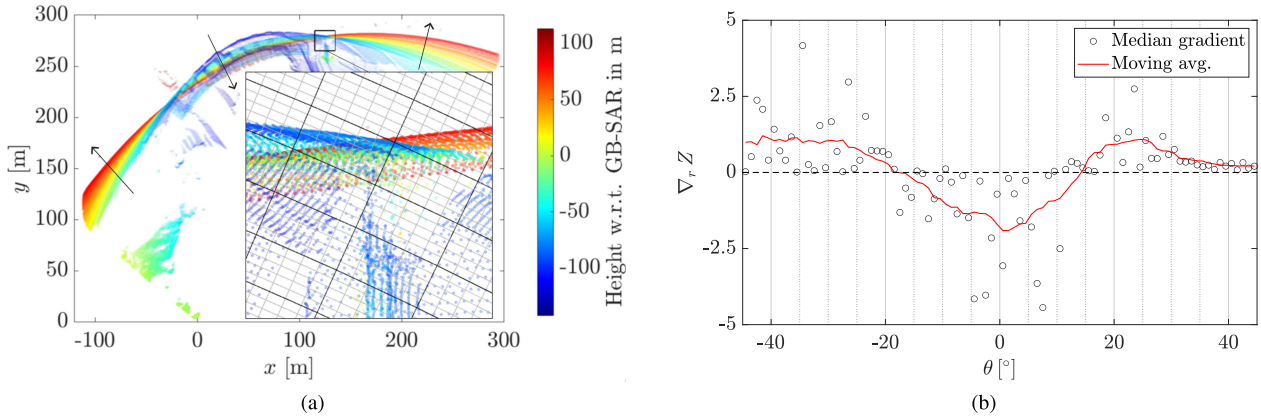

Fig. 4. Analysis of the range dependent elevation gradient (a) P-RaySAR points projected in the SAR geometry. Arrows indicate the elevation gradient in this geometry with inversed trend (overlay) in the central part. (b) Median of $\nabla_r Z$ as a function of the cross-range angle.

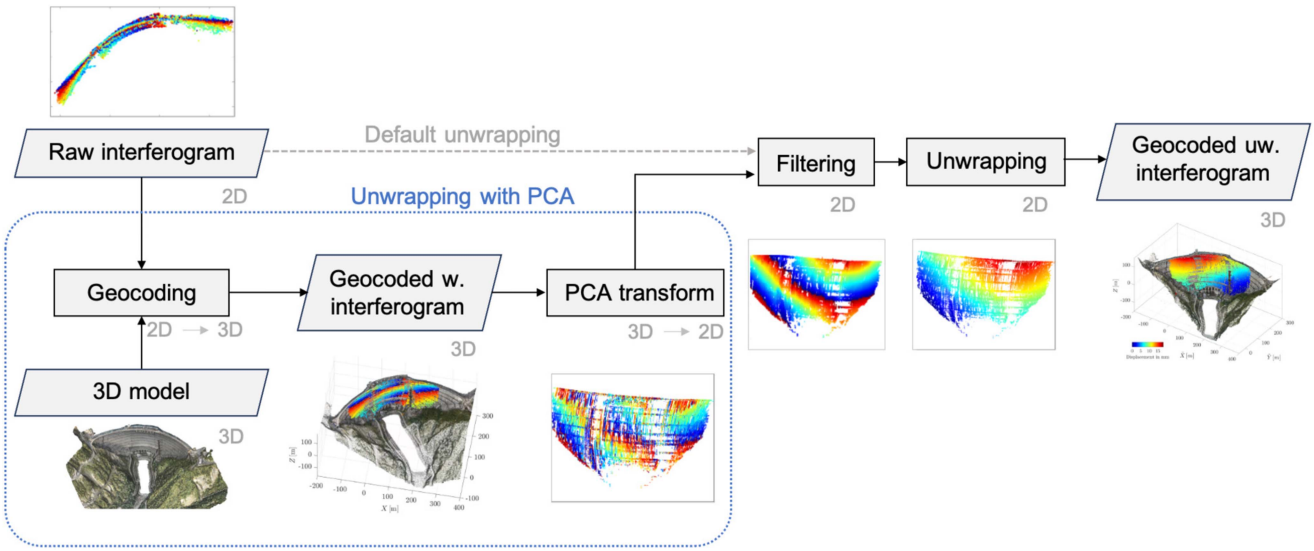

Fig. 5. Flowchart of the proposed method to unwrap GB-SAR interferograms in a more suitable geometry.

tensor, providing insights into the structure of the input 3-D point cloud. In our study, the geocoded 3-D point cloud of the PS is used as input and is represented by the set of coordinates $\mathbf{X}_{\text{PS}} = [X_{\text{PS},k}, Y_{\text{PS},k}, Z_{\text{PS},k}]_{k\in[1:N_{\text{geo}}]} \in \mathbb{R}^3$.

Subsequently, the dispersion of the points from the center of the scenario $\bar{\mathbf{X}}_{\text{PS}}$ along each axis is computed using the structure tensor $\mathbf{S} \in \mathbb{R}^{3\times3}$ via

$$\mathbf{S} = \frac{1}{N_{\text{geo}}} \sum_{k=1}^{N_{\text{geo}}} \left(\mathbf{X}_{\text{PS},k} - \bar{\mathbf{X}}_{\text{PS}}\right)\left(\mathbf{X}_{\text{PS},k} - \bar{\mathbf{X}}_{\text{PS}}\right)^{\mathsf{T}}. \tag{5}$$

Due to its computation, $\mathbf{S}$ is a symmetric positive-definite matrix and it is possible to compute its eigenvalues and eigenvectors using the principal component analysis (PCA). The result of the PCA is the decomposition of $\mathbf{S}$ into the product of three matrices

$$\mathbf{S} = \mathbf{W}\mathbf{\Lambda}\mathbf{W}^{\mathsf{T}} \tag{6}$$

with $\mathbf{W} \in \mathbb{R}^{3\times3}$ composed of the eigenvectors $\mathbf{w_1}, \mathbf{w_2}, \mathbf{w_3}$ of $\mathbf{S}$ and $\mathbf{\Lambda} = \text{diag}(\Lambda_1, \Lambda_2, \Lambda_3) \in \mathbb{R}^{3\times3}$ the diagonal matrix with the corresponding eigenvalues. The two eigenvectors corresponding to the two largest eigenvalues are the two main directions of the corresponding point cloud. To project the points onto the plane, spanned by these eigenvectors, the projection matrix is given by $\mathbf{W}_{\text{2D}} = [\mathbf{w_1}, \mathbf{w_2}]$. The new 2-D coordinates vector $\mathbf{x}_{\text{PCA}}$ is given with

$$\mathbf{x}_{\text{PCA}}^{\mathsf{T}} = \mathbf{X}_{\text{PS}}^{\mathsf{T}} \mathbf{W}_{\text{2D}}. \tag{7}$$

Fig. 5 illustrates the steps for processing the input interferogram shown in Fig. 3(a). The raw interferogram is presented in the upper left part of the chart. The first step implies the geocoding of the wrapped interferogram, which is then available in 3-D. The PCA transformation based on the geometry of the geocoded PS points leads to another 2-D interferogram available under the *PCA transform* box. Therefore, the input interferogram for filtering and unwrapping is much more expanded. The filtering and unwrapping steps are represented under their respective box.

The transformation expands the size of the fringes in a wrapped interferogram, resulting in a more representative 2-D

image of the signal. By extracting the two main components of the PCA geometry, we obtain a rotated coordinate system that encapsulates the most pertinent geometric information of the observed 3-D scenario in two dimensions. A valuable quantity when computing principal components is the cumulative explained variance (CEV), computed in this specific case as

$$\mathrm{CEV} = \frac{\Lambda_1 + \Lambda_2}{\mathrm{tr}(\mathbf{\Lambda})} \in [0; 1]. \tag{8}$$

It is an indicator of how much of the data's dispersion is retained up to the considered order of the PCA. The value of the CEV for the principal plane for the station considered in the case study is about $95\,\%$ of the data, ensuring a projection coordinate system with almost no layover or foreshortening effects.

To quantify the amount of information earned with the transformation, the area contained in the convex hull of the PS is evaluated for both geometries. In the classical SAR geometry this area equals $9.5 \cdot 10^3\,\mathrm{m}^2$, while in the PCA geometry this area is equal to $6.23 \cdot 10^4\,\mathrm{m}^2$, corresponding to a ratio of 7 and a considerable reduction of the foreshortening. Even in the PCA geometry, the GB-SAR scenes contain a significant amount of noise after several months between the interferograms. The output interferograms are resampled using a pixel size of 4 m and the Goldstein filter [24] is applied with a factor $\alpha = 1$. The algorithm for the phase unwrapping can be any of the 2-D classical workflows. For the presented results of this work, SNAPHU [12] is applied on the resampled interferograms, as a fast and reliable phase unwrapping algorithm. The version used is 2.0.4, with the cost computation based on the smooth-solution assumption.

IV. Results

A. Consistency Analysis

As the station has only the dam in its field of view, the PCA plane is almost parallel to the main directions of the dam. It enables a continuous consistency on the observed signal with respect to the physical deformation process of the dam. However, the PCA transformation does not increase the original GB-SAR resolution and its primary purpose is to improve the representation of the deformation signal. The implemented Goldstein filter enables to synthetically enhance the resolution based on its patch size, at the cost of the ability to detect nonsmooth spatial patterns.

The geocoded displacement results after phase unwrapping for this station, as represented in Fig. 6, are quite revealing. For this figure, each line corresponds to the wrapped interferogram presented in Fig. 3.

In the map generated using the classical SAR geometry for the case of Fig. 6(a), two major discontinuities arise. Those discontinuities happen at the location where the phase gradient changes its sign in Fig. 4(b). The results with the proposed geometry presented in Fig. 6(b) lead to an unwrapped signal that is continuous and physically more consistent across the entire dam. The results of the unwrapping in the classical geometry could eventually be used by dividing the dam into three parts, analyzing each one independently and correcting the discontinuities manually. For the second case represented in Fig. 6(c) and (d), with a much denser signal, there is nothing interpretable when the signal is not processed using the PCA geometry. For the last case in Fig. 6(e) and (f), it shows that even a simple signal in the SAR geometry cannot be well recovered with the classical processing, while the recovered displacement map is more likely to be correct using the proposed method, due to its continuity.

The available dataset contains five campaign measurements, resulting in ten possible different interferograms. The computation of residual phases in closed-loop combinations of these interferograms enables to quantify the number of inconsistencies and therefore unwrapping errors, as detailed in [25].

Considering three SAR images indexed with the numbers 1, 2, 3 and the corresponding interferograms I_{1-2}, I_{1-3}, and I_{2-3}, the closed-loop C value is computed for each pixel in via

$$C = I_{1-2} + I_{2-3} - I_{1-3}. \tag{9}$$

In the case of one or several unwrapping errors in the closed loop, multiples of 2π appear. The unwrapping has been applied to all the interferograms with the classical and the proposed method. The histograms of the residuals are available in Fig. 7. The noninteger residuals are due to the Goldstein filter. The proposed method offers a better consistency than unwrapping in the classical geometry, as the peak centered on zero is much more prominent. Moreover, no significant unwrapping error larger than 2π is observed.

B. Atmospheric and Repositioning Correction

For a subsequent comparison with other displacement maps, the temporal variable phase contributions from changing atmospheric phase delay and repositioning errors should be removed as much as possible. The two contributions are addressed by the combined term of disturbance phase hereinafter. Although meteorological sensors were installed at a later time, for the considered data stack of campaign-based GB-SAR acquisitions there are no meteorological observations available that could be used to eliminate the atmospheric phase contributions. Therefore, only a spatial model can be fitted for the atmospheric phase. Several models exist, as presented in [26], [27], [28], [29], or [30], with different parameters. In this work, the range-elevation model as developed in [27] is applied. Indeed, the elevation differences at the dam are large, meaning that a model considering the elevation effect of the atmosphere is required. However, due to the short range between the dam and the radar, more complex models with azimuth parameters are not necessary. For the error due to the repositioning of the instrument between the campaigns, the model developed in [31] is applied. The disturbing signal is then expressed as the sum of both contributions and is denoted with $\phi_{\text{dist.}}$

$$\phi_{\text{dist.}} = \underbrace{C_0 + C_1 r + C_2 r Z}_{\text{Atmospheric signal}} + \underbrace{C_3 \frac{X}{r} + C_4 \frac{Y}{r} + C_5 \frac{Z}{r}}_{\text{Repositioning error}} \tag{10}$$

where $X, Y, Z,$ and r are the coordinates of the points relative to the GB-SAR, r being the range. C_k are the estimated coefficients using a two-step least-squares estimator as in [27]. Typically,

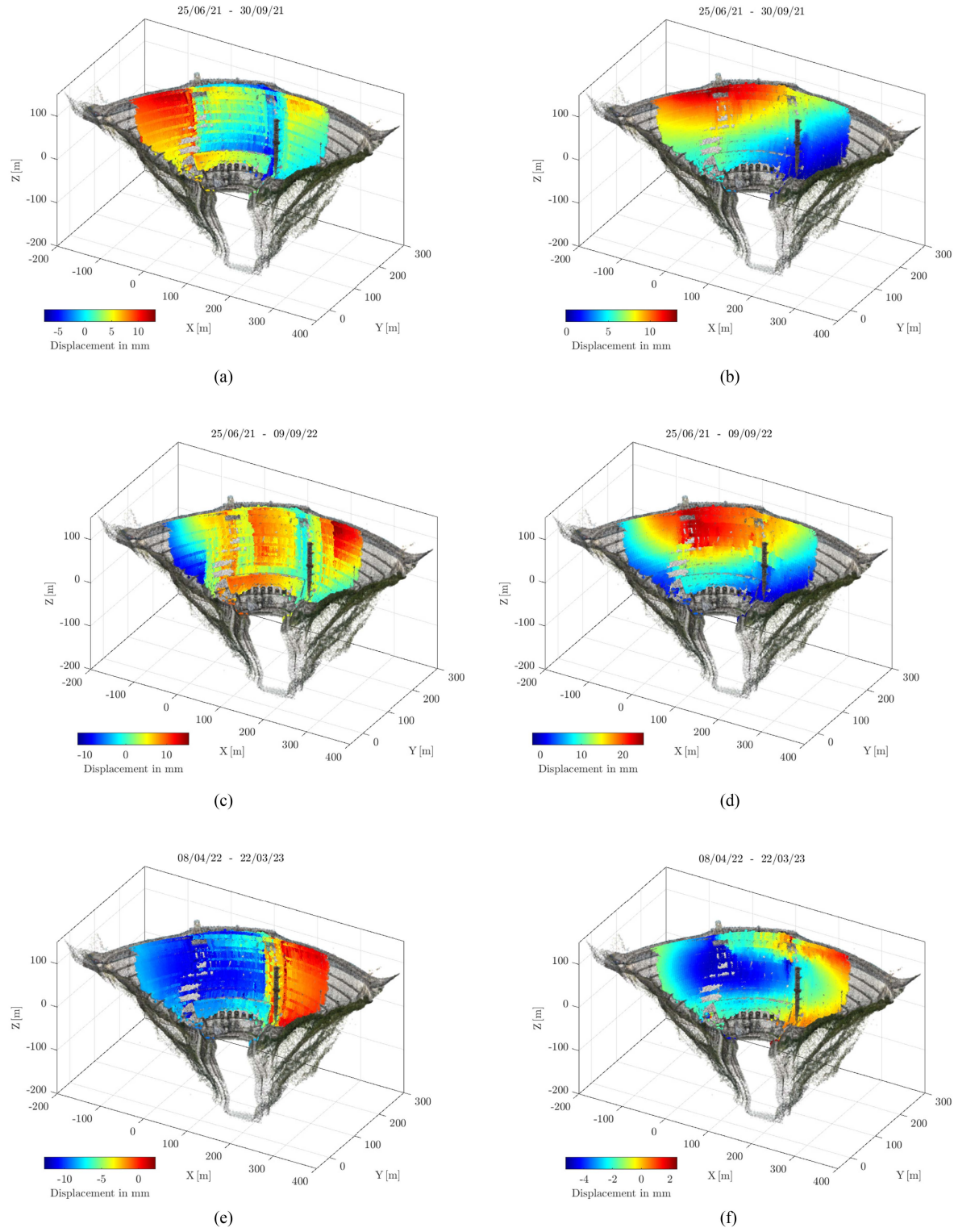

Fig. 6. Results from the phase unwrapping. (a) Unwrapping in SAR geometry - Case 1. (b) Unwrapping in PCA geometry - Case 1. (c) Unwrapping in SAR geometry - Case 2. (d) Unwrapping in PCA geometry - Case 2. (e) Unwrapping in SAR geometry - Case 3. (f) Unwrapping in PCA geometry - Case 3.

the atmospheric phase signal is estimated at a reference area that is expected to be stable over time without any deformation signal. However, the field of the presented station only covers the unstable area of the dam, meaning that there is no possibility to estimate the disturbance model on a stable area for this station.

Therefore, a specific reference approach is needed to adequately fit this signal. For each campaign, two observations have been acquired from the same position but with different azimuth viewing orientations. Between these observations, the GB-SAR was rotated around the vertical axis with the position of the center

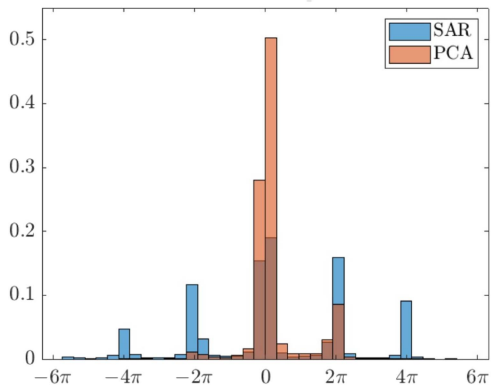

Fig. 7. Histogram of the closed-loop residuals.

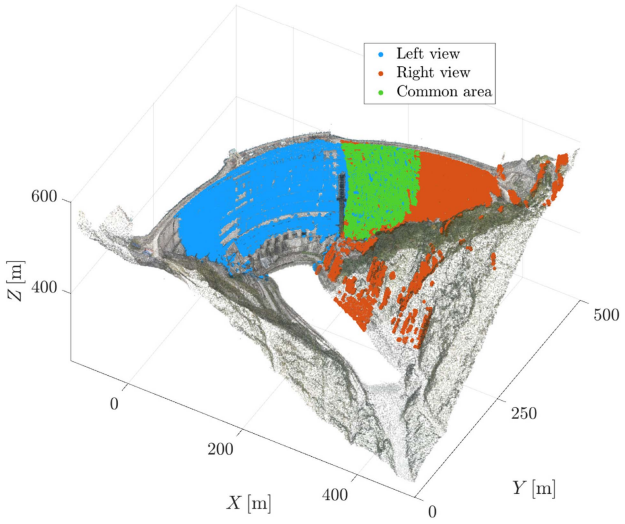

Fig. 8. Common area of the two stations. The red and blue parts correspond to the PS points from the right and left view, respectively. The green points are visible from both orientations.

of the radar preserved with mm accuracy. Both acquisitions, namely a left and a right view, have a partial visibility on the dam that overlaps in its central part. Fig. 8 represents the visibility given by both viewing angles of the station. The green part corresponds to the overlapping area on the dam. The points on the right view acquisition can be divided into three groups: 1) stable points on the rock ($\mathcal{A}_R$); 2) points on the dam not visible from the left view ($\mathcal{B}_R$); and 3) points on the dam visible in the left and right view ($\mathcal{C}_R$). In the same way, it is possible to group the points from the left view into two categories: 1) points on the dam not visible from the right view ($\mathcal{B}_L$); and 2) points on the dam visible from the left and right view ($\mathcal{C}_L$). Although points from ($\mathcal{C}_R$) and ($\mathcal{C}_L$) are not necessarily homologous points, they are located at the same area.

The interferograms generated from the right view acquisitions are corrected using the surrounding stable rocks, i.e., points from $\mathcal{A}_R$, with the previously mentioned spatial model. Then, the whole set of right view interferograms can be considered error-free in a first approximation. Subsequently, the points $\mathcal{C}_R$ are used to correct disturbance phase of the interferograms from the left view.

To do this, for each point of $\mathcal{C}_L$, we identify the closest point belonging to $\mathcal{C}_R$, with a maximal tolerance of 2 m. Therefore, for each of the green points in Fig. 8, there are two phase values available, the one from the corrected interferogram from the right view $\tilde{\phi}_R$, and the one from the uncorrected interferogram from the left view ϕ_L. These two terms can be, respectively, written as follows:

$$\begin{aligned} \phi_L &= \phi_{\mathrm{d}} + \phi_{\mathrm{dist.},L} + \phi_{\mathrm{n},L} \\ \tilde{\phi_R} &= \phi_{\mathrm{d}} + \phi_{\mathrm{n},R} \end{aligned} \tag{11}$$

with ϕ_{d} the displacement signal, $\phi_{\mathrm{dist.}}$ the disturbance signal, and ϕ_{n} is the remaining noise. The L and R indexes are, respectively, from the left and right view interferograms. As the right view signal can be corrected, we already have access to corrected values $\tilde{\phi_R}$. The vector of differences $\tilde{\phi_R} - \phi_L$ is then used to feed the model of (10) and estimate the disturbance signal from the right view with the least squares method previously mentioned. Once corrected, a combined displacement map with reduced disturbance phase is available for the whole dam.

The results presented in Fig. 9 highlight why the correction of the signal is necessary and how important the effect is. As already described with Fig. 8, the interferograms corresponding to the right view can be corrected using the surrounding stable areas. As the left view has only the dam in visibility, it is not directly possible to correct it. Fig. 9(a) shows the superposition of the corrected right view interferogram and the uncorrected left view interferogram. It is clear that there is an aliasing effect on the common area. After the correction, there is no aliasing anymore and moreover, the signal trend corresponding to atmosphere and repositioning error that was present, has been removed. The displacement pattern is much more likely to a displacement map, as it is much more symmetric with respect to the dam's center.

C. Comparison With a Numerical Model

The estimated displacement is compared to a numerical model and the results are presented in Fig. 10. The numerical model contains a 3-D mesh of the dam associated with physical parameters like the Young's modulus. These parameters are adjusted based on plumbline data available from 2000 to 2019. Eight full lines are built, with displacement values available with very high accuracy of 0.1 mm. More information about the computation of the model and its comparison with GB-SAR measurements can be found in [6] and [23]. According to this comparison, the model is well calibrated and generally in very good agreement to the measured displacements from plumbline data, but can deviate up to 30%.

External forces are applied to the calibrated model to simulate the dam deformation. Subsequently, a displacement map in the GB-SAR line-of-sight can be computed from different loading scenarios of the dam. To achieve a meaningful comparison with the GB-SAR, the hydrostatic pressure computed with the water levels at the acquisition times is applied. As no temperature data were collected, the thermal dilation is obtained with the average temperature-related deformation calibrated over the 19 years

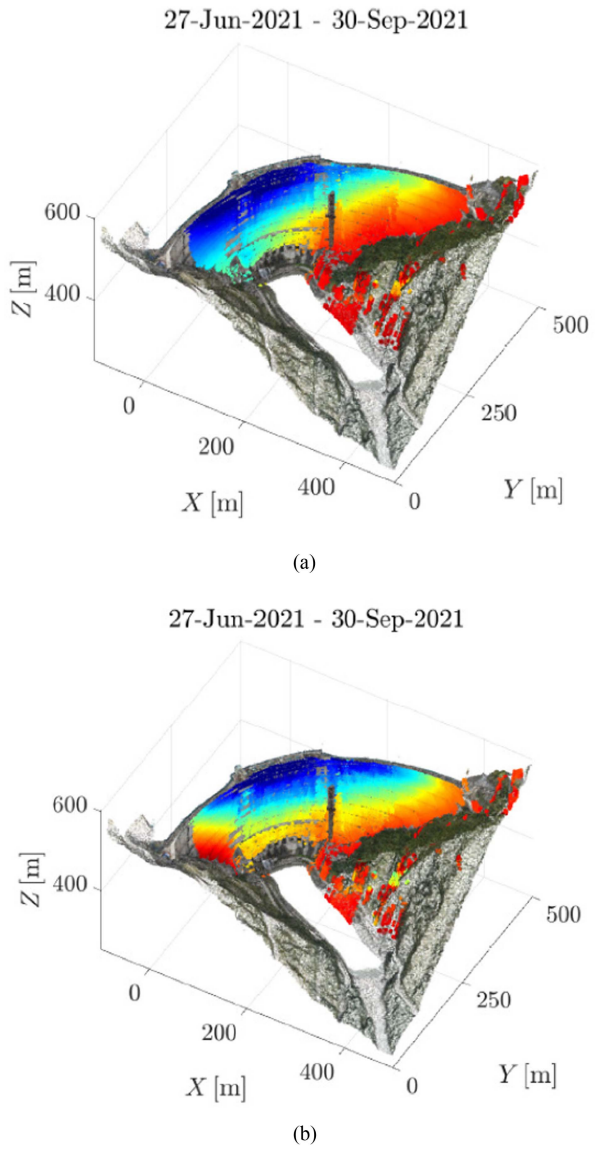

Fig. 9. Effect of the atmospheric and repositioning correction on the left view. (a) Right interferogram is corrected but not the left one. (b) Left interferogram is corrected using the overlapping area of both interferograms.

of plumbline data. The forces applied to the numerical model correspond to the hydrostatic-season-temporal model [32], [33].

Two cases are presented: the first one presents the deformation observed and modeled between the conditions in June 2021 and September 2021 (492.7 and 482.0 m of water level, respectively); the second case represents the observed deformation between June 2021 and September 2022 (492.7 and 453.0 m of water level, respectively).

In Fig. 10(a) and (b), the projected displacement computed by the respective numerical models along the line-of-sight of the radar is presented. In both cases, a negative displacement corresponds to a movement of the dam toward the radar. The displacement pattern is not centered for two major reasons as follows.

1) This concrete arch dam withstands the force of the water reservoir by transferring it to the rock formations on its left and right sides. Physical seismic measurements and rock analyses have shown that the rock on the left side (when facing the dam) is significantly weaker than the rock on the right. As a result, the left side provides less support, leading to greater movement in that area.
2) The deformation pattern observed is the projection of the 3-D displacement vectors, calculated by the model, onto the radar's line-of-sight. This projection is different for each point on the dam and influences the apparent magnitude of the deformation.

The general agreement between the results of the GB-SAR processing and the numerical model is high, as the majority of the absolute relative differences on the dam is lower than 30%, which is in the range of maximum deviation between the model and the plumblines. On both difference maps, the right part of the dam shows lower deformation in the numerical model than observed by GB-SAR, which can be due to the plumbline not reaching the dam's crest in this area. This implies that no displacement values are available to calibrate the material properties of the model. Moreover, the very low displacement values accentuate the relative error. In the first case, a major difference exists between both deformation maps at the dam's crest. This effect can be due to significant thermal differences between the average temperature computed between 2000 and 2019 used for the calibration, and the temperature at the GB-SAR acquisitions in 2021 and 2022. Indeed, no temperature data were available for the years during the GB-SAR acquisitions. Therefore, the thermal conditions applied to the model are based on the averaged temperature of 2000–2019 at the day of the year corresponding to the GB-SAR acquisitions. This approximation could lead to several millimeters of difference. As the modeled displacement shows a maximum magnitude of only 1 cm at the dam crest, it could explain the observed difference. For more details on the influence of the thermal effects on the dam with respect to the model used see [34].

V. Discussion

The proposed method has been developed to monitor the deformation of a dam using a GB-SAR with complex imaging geometry. It shows that even in the case of strong foreshortening and layover effects, it is possible to extract the relevant information by adopting the processing strategy for phase unwrapping.

With reprojecion of the observed data from SAR imaging geometry to the optimized PCA-plane, the distortion effects from SAR imaging geometry are significantly reduced, proven by the significant expansion of the convex hull. However, although the dam is mapped on a larger image area, the methodology does not increase the resolution provided by the hardware, and an interpretable image in PCA geometry is obtained via filtering. Therefore, the methodology is well suited for large and reasonably smooth deformation patterns. However, in the case of localized deformation, i.e., with small extent compared to the spatial resolution, this methodology may not recover the full signal due to the spatial filtering. A remove-restore approach may be a suitable compromise in this case, with first unwrapping the large-scale deformation in PCA-geometry to account for the

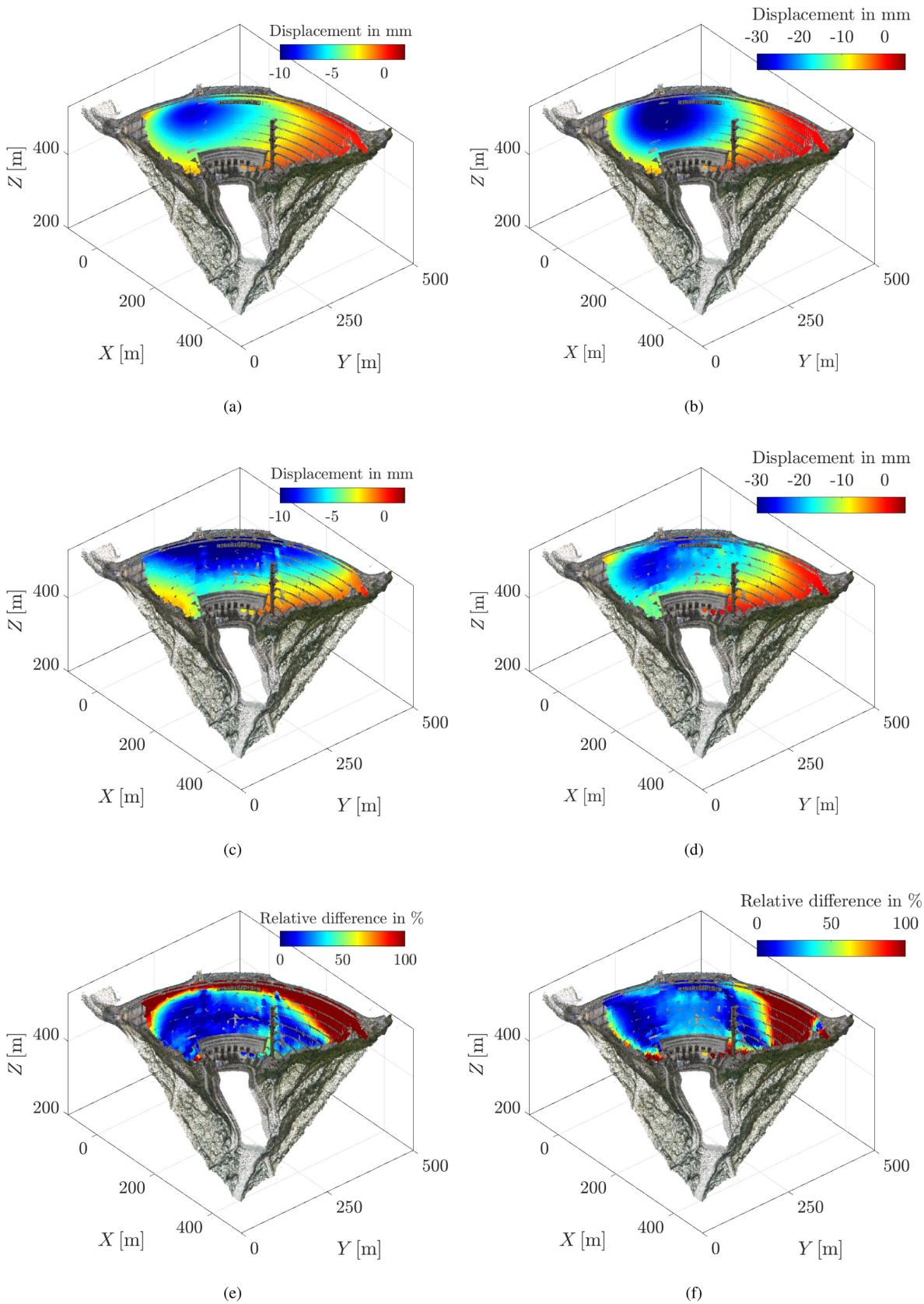

Fig. 10. Comparison between the numerical model and the GB-SAR displacement maps. Case 1 with $\tilde{1}0$ – m water level change: (a) Modeled displacement (c) Observed displacement (e) Absolute relative difference. Case 2 with $\tilde{1}0$ m water level change: (b) Modeled displacement (d) Observed displacement (f) Absolute relative difference.

geometric distortion and subsequently unwrapping the residuals in the original SAR imaging geometry.

The presented results in this study express that the proposed methodology is efficient in extracting displacement even in the worst scenario for a radar, when the object surface has a shape that is parallel to the wavefront at different locations with reversing phase gradients in the image. We see a broader range of application in SAR imaging, whenever complex imaging geometry with changing layover and foreshortening hampers phase unwrapping.

For satellite SAR applications, this approach can be considered to enable phase unwrapping and reduce unwrapping errors in cases of local-scale studies or high-resolution imaging of single objects like dams or mountain slopes. For studies on a regional scale, it is barely the case that the whole monitored area has a strongly distorted imaging geometry. Therefore, by processing locally on a patch-based approach, it can be extended to such scenarios, offering enhanced results.

VI. Conclusion

The proposed method introduces a geometric transformation of SAR interferograms to a PCA-based geometry which is more favorable for phase unwrapping. The transformation is based on the geocoded set of 3-D coordinates of PS points. Using this point cloud, the PCA is applied to identify the plane in 3-D space that contains the majority of the data's dispersion.

In the complex environment of the Enguri Dam, this approach demonstrates a substantial improvement in the unwrapped results. The output is a smooth and continuous signal mapped across the entire dam, whereas unwrapping in the classical geometry leads to discontinuities. However, it is important to note that the use of this method requires an analysis of the transformed coordinates to ensure that different 3-D points are not projected onto the same 2-D coordinates, which could result in information superposition.

The presented approach is especially helpful in cases where the interferometric phase is substantial and phase unwrapping of the signal cannot be bypassed by remove-restore approaches with modeled signal components.

Two deformation maps have been presented and compared to a numerical simulation. The agreement between the model and the GB-SAR processed results is satisfying, especially considering the complexity of the input raw data.

References

[1] M. Scaioni, M. Marsella, M. Crosetto, V. Tornatore, and J. Wang, "Geodetic and remote-sensing sensors for dam deformation monitoring," *Sensors*, vol. 18, no. 11, 2018, Art. no. 3682. [Online]. Available: https://www.mdpi.com/1424-8220/18/11/3682

[2] D. Tarchi, H. Rudolf, G. Luzi, L. Chiarantini, P. Coppo, and A. J. Sieber, "SAR interferometry for structural changes detection: A demonstration test on a dam," in *Proc. IEEE Int. Geosci. Remote Sens. Symp.*, 1999, vol. 3, pp. 1522–1524.

[3] M. Alba et al., "Measurement of dam deformations by terrestrial interferometric techniques," *Int. Arch. Photogramm. Remote Sens. Spat. Inf. Sci.*, vol. 37, no. B1, pp. 133–139, 2008.

[4] M. Jacquemart and L. Meier, "Deformationsmessungen an talsperren und in deren alpiner umgebung mittels radarinterferometrie," *Wasser Energie Luft*, vol. 106, pp. 105–111, 2014.

[5] A. Wieser, S. Condamin, V. Barras, L. Schmid, and J. Butt, "Staumauerüberwachung–vergleich dreier technologien für epochenweise deformationsmessungen," in *Proc. Ingenieurvermessung 20. Beiträge zum 19. Internationalen Ingenieurvermessungskurs München*, 2020, pp. 437–449.

[6] M. Rebmeister, A. Schenk, S. Hinz, F. Andrian, and M. Vonie, "High dam monitoring with ground-based SAR: Opportunities and challenges," in *Proc. 91st ICOLD Annu. Meeting*, 2023, pp. 1409–1418.

[7] Z. Qiu, M. Jiao, T. Jiang, and L. Zhou, "Dam structure deformation monitoring by GB-InSAR approach," *IEEE Access*, vol. 8, pp. 123287–123296, 2020.

[8] P. Wang, C. Xing, and X. Pan, "Reservoir dam surface deformation monitoring by differential GB-InSAR based on image subsets," *Sensors*, vol. 20, no. 2, 2020, Art. no. 396. [Online]. Available: https://www.mdpi.com/1424-8220/20/2/396

[9] C. Wolff, M.-H. Derron, C. Rivolta, and M. Jaboyedoff, "A tool for estimating ground-based InSAR acquisition characteristics prior to monitoring installation and survey and its differences from satellite InSAR," *Geoscientific Instrum., Methods Data Syst.*, vol. 13, no. 2, pp. 225–248, 2024.

[10] M. Rebmeister, S. Auer, A. Schenk, and S. Hinz, "Geocoding of ground-based SAR data for infrastructure objects using the maximum a posteriori estimation and ray-tracing," *ISPRS J. Photogrammetry Remote Sens.*, vol. 189, pp. 110–127, 2022.

[11] M. Costantini, A. Farina, and F. Zirilli, "A fast phase unwrapping algorithm for SAR interferometry," *IEEE Trans. Geosci. Remote Sens.*, vol. 37, no. 1, pp. 452–460, Jan. 1999.

[12] C. W. Chen and H. A. Zebker, "Two-dimensional phase unwrapping with use of statistical models for cost functions in nonlinear optimization," *J. Opt. Soc. Amer. A*, vol. 18, no. 2, pp. 338–351, 2001.

[13] M. Crosetto, O. Monserrat, G. Luzi, M. Cuevas-González, and N. Devanthéry, "Discontinuous GBSAR deformation monitoring," *ISPRS J. Photogrammetry Remote Sens.*, vol. 93, pp. 136–141, 2014.

[14] C. Magnard, U. Wegmüller, and C. Werner, "Persistent scatterer interferometry in mountainous areas: Advantages of working in map geometry," *Procedia Comput. Sci.*, vol. 181, pp. 198–205, 2021.

[15] L. Schmid, T. Medic, B. D. Collins, L. Meier, and A. Wieser, "Georeferencing of terrestrial radar images in geomonitoring using kernel correlation," *Int. J. Remote Sens.*, vol. 44, no. 21, pp. 6736–6761, 2023.

[16] A. Hooper, P. Segall, and H. Zebker, "Persistent scatterer interferometric synthetic aperture radar for crustal deformation analysis, with application to volcán alcedo, galápagos," *J. Geophysical Research: Solid Earth*, vol. 112, no. B7, 2007, Art. no. B07407.

[17] A. Ferretti, C. Prati, and F. Rocca, "Permanent scatterers in SAR interferometry," *IEEE Trans. Geosci. Remote Sens.*, vol. 39, no. 1, pp. 8–20, Jan. 2001.

[18] Z. Wang, Z. Li, and J. P. Mills, "A new nonlocal method for ground-based synthetic aperture radar deformation monitoring," *IEEE J. Sel. Topics Appl. Earth Observ. Remote Sens.*, vol. 11, no. 10, pp. 3769–3781, Oct. 2018.

[19] K. V. Mardia, P. E. Jupp, and K. Mardia, *Directional Statistics*, vol. 2. Hoboken, NJ, USA: Wiley Online Library, 2000.

[20] W. Tian, Z. Zhao, C. Hu, J. Wang, and T. Zeng, "GB-InSAR-based DEM generation method and precision analysis," *Remote Sens.*, vol. 11, no. 9, 2019, Art. no. 997.

[21] M. Pieraccini and L. Miccinesi, "Ground-based radar interferometry: A bibliographic review," *Remote Sens.*, vol. 11, no. 9, 2019, Art. no. 1029.

[22] M. Weinmann, B. Jutzi, S. Hinz, and C. Mallet, "Semantic point cloud interpretation based on optimal neighborhoods, relevant features and efficient classifiers," *ISPRS J. Photogrammetry Remote Sens.*, vol. 105, pp. 286–304, 2015.

[23] M. Rebmeister, "Geodetic monitoring of complex shaped infrastructures using ground-based InSAR," Ph.D. dissertation, Karlsruher Institut für Technologie (KIT), Karlsruhe, Germany, 2024.

[24] R. M. Goldstein and C. L. Werner, "Radar interferogram filtering for geophysical applications," *Geophysical Res. Lett.*, vol. 25, no. 21, pp. 4035–4038, 1998.

[25] F. Falabella and A. Pepe, "On the phase nonclosure of multilook SAR interferogram triplets," *IEEE Trans. Geosci. Remote Sens.*, vol. 60, 2022, Art. no. 5120117.

[26] L. Noferini et al., "Permanent scatterers analysis for atmospheric correction in ground-based SAR interferometry," *IEEE Trans. Geosci. Remote Sens.*, vol. 43, no. 7, pp. 1459–1471, Jul. 2005.

[27] R. Iglesias et al., "Atmospheric phase screen compensation in ground-based SAR with a multiple-regression model over mountainous regions,"

IEEE Trans. Geosci. Remote Sens., vol. 52, no. 5, pp. 2436–2449, May 2014.
[28] Y. Izumi, L. Zou, K. Kikuta, and M. Sato, "Iterative atmospheric phase screen compensation for near-real-time ground-based InSAR measurements over a mountainous slope," *IEEE Trans. Geosci. Remote Sens.*, vol. 58, no. 8, pp. 5955–5968, Aug. 2020.
[29] N. Dematteis, G. Luzi, D. Giordan, F. Zucca, and P. Allasia, "Monitoring alpine glacier surface deformations with GB-SAR," *Remote Sens. Lett.*, vol. 8, no. 10, pp. 947–956, 2017.
[30] J. Liu, H. Yang, L. Xu, and T. Li, "Novel model-based approaches for non-homogenous atmospheric compensation of GB-InSAR in the azimuth and horizontal directions," *Remote Sens.*, vol. 13, no. 11, 2021, Art. no. 2153.
[31] C. Hu, J. Zhu, Y. Deng, W. Tian, and P. Yin, "Repositioning error compensation in discontinuous ground-based SAR monitoring," *Remote Sens.*, vol. 13, no. 13, 2021, Art. no. 2461.
[32] G. Willm and N. Beaujoint, "Les méthodes de surveillance des barrages au service de la production hydraulique d'électricité de France. problèmes anciens et solutions nouvelles," in *Proc. 9th Int. Congr. Large Dams*, 1967, pp. 529–550.
[33] F. Salazar, R. Morán, M. Á. Toledo, and E. Oñate, "Data-based models for the prediction of dam behaviour: A review and some methodological considerations," *Arch. Comput. Methods Eng.*, vol. 24, pp. 1–21, 2017.
[34] M. Tatin, M. Briffaut, F. Dufour, A. Simon, and J.-P. Fabre, "Statistical modelling of thermal displacements for concrete dams: Influence of water temperature profile and dam thickness profile," *Eng. Structures*, vol. 165, pp. 63–75, 2018.

Matthieu Rebmeister received the Engineer degree in surveying from the National Institute of Applied Sciences, Strasbourg, France, and the M.Sc. degree in geodesy and geoinformatics and the Ph.D. degree in geodesy from the Institute of Photogrammetry and Remote Sensing, Karlsruhe Institute of Technology, Karlsruhe, Germany, in 2020 and 2024, respectively.

Since 2024, he has been with Leica Geosystems - Part of Hexagon, Heerbrugg, Switzerland, where he works as a Product Engineer with the product management team for total station innovations.

Andreas Schenk received the diploma degree in applied geophysics from TU Berlin, Berlin, Germany, in 2006, and the Ph.D. degree in geodesy from the Geodetic Institute, Karlsruhe Institute of Technology, Karlsruhe, Germany, in 2015.

Since 2015, he has been with the Institute of Photogrammetry and Remote Sensing, Karlsruhe Institute of Technology. His research interests include remote sensing methods and retrieval of geophysical variables from hyperspectral and radar remote sensing

Stefan Hinz received the Ph.D. and venia legendi (Habilitation) degrees in computer vision and remote sensing from the Technical University of Munich, Munich, Germany, in 2003 and 2008, respectively.

In 2008, he became a Full Professor and the Director of the Institute of Photogrammetry and Remote Sensing, Karlsruhe Institute of Technology, Karlsruhe, Germany. His research interests include theory and methods of computer vision and remote sensing, with particular focus on semantic image understanding, image sequence analysis, hyperspectral, and radar remote sensing.

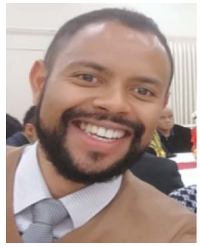

Frédéric Andrian recevied the M.Eng. degree in civil engineering from the Joseph Fourier University of Grenoble, France, in 2004.

He is currently a Project Director for the Dams, Hydropower and Infrastructures Business Unit with Artelia, Saint-Ouen-sur-Seine, France. He leads the design, safety review, or refurbishment studies mostly for concrete dams and their appurtenant structures. He is currently the Manager of the Structural & Numerical Analysis team for Civil Engineering and Geomechanics.

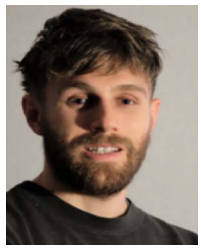

Maxime Vonié received the M.Eng. degree in civil engineering with the INSA National Institute of Applied Sciences, Lyon, France, in 2021.

He is currently a Civil Engineer for the Dams, Hydropower and Infrastructures Business Unit with Artelia, Saint-Ouen-sur-Seine, France. He specializes in numerical and structural analyses, stability analyses as well as monitoring analyses mostly for concrete dams and their appurtenant structures.